Cluster correlations for low-lying intruder states of ^{12}Be

M. Ito,[1,2,3] N. Itagaki,[4] and K. Ikeda[3]

[1]*Department of Pure and Applied Physics, Kansai University, Yamatecho, 3-3-35 Suita, Japan*

[2]*Research Center for Nuclear Physics (RCNP), Osaka University, Mihogaoka 10-1, Suita 567-0047, Japan*

[3]*RIKEN Nishina Center for Accelerator-Based Science, RIKEN, Wako, 351-0198 Saitama, Japan*

[4]*Yukawa Institute for Theoretical Physics (YITP), Kyoto University, Kyoto 606-8502, Japan*

(Received 5 May 2011; published 4 January 2012)

The formation of intruder states in the low-lying states of $^{12}\mathrm{Be} = \alpha + \alpha + 4N$ is studied by applying the generalized two-center cluster model, which can optimize the excess neutrons' orbits depending on the α-α distance. The correlation energy for the intruder states is analyzed from the viewpoint of two different pictures based on the cluster structure: the covalent picture around two α clusters and the binary He-cluster picture. In the covalent picture, the binding energy of $(\pi^-_{3/2})^2(\sigma^+_{1/2})^2$, corresponding to $\nu(0p)^4(1s0d)^2$ in a naive shell model, gains largely owing to the spin-triplet pairing of the $0d$-wave neutrons, which is induced by the two-body spin-orbit interaction. The spin-triplet pairing gives rise to the reduction of the kinetic energy and the increase of the attractive spin-orbit interaction for the excess neutrons. As a result of these correlation energies, the $\nu(0p)^4(1s0d)^2$ configuration becomes dominant in the ground state. In the binary cluster picture, the correlation energy is investigated from the coupled channels among $\alpha + {}^8$He, ^{6}He + ^{6}He, and ^{5}He + ^{7}He. The coupling to ^{5}He + ^{7}He, which is neglected in usual binary-cluster models, plays an important role for a large reduction of kinetic energy and the formation of a pair of the low-lying 0^+ states with a close energy spacing recently observed in experiment. The rotational bands are also discussed from the viewpoint of these two cluster pictures.

DOI: 10.1103/PhysRevC.85.014302 PACS number(s): 21.60.Gx, 24.10.Eq, 25.60.Je, 27.20.+n

I. INTRODUCTION

The molecular structures in nuclei are one of the characteristic structures established in a wide range of $N = Z$ nuclei [1]. Typical examples are the binary molecular structure of a ground band in $^8\mathrm{Be} = \alpha + \alpha$ and a three-α structure in 0^+_2 of ^{12}C at 7.65 MeV called the Hoyle state. An α particle is a quite stable and inert nucleus owing to the strong binding of two protons and two neutrons forming a spin-isospin saturated state. Therefore, α particles can be considered as possible building blocks of light $N = Z$ systems. We can see some examples on multi-α states in recent studies of the molecular resonances in high-spin regions [2] and gaslike states [3,4].

However, in the last two decades, developments of experiments with a secondary radioactive ion beam have extensively helped the studies on light neutron-rich ($N > Z$) nuclei. The cluster degrees of freedom are important not only in the $N = Z$ systems, but also in the $N > Z$ ones. In isotope chains of the elements, Be, B, C, and Ne, for instance, structures of low-lying states were systematically studied, and the appearance of various cluster structures were pointed out [5]. In particular, much effort has been devoted to the molecular structure in Be isotopes. In recent experiments, exotic structures of these isotopes have been studied and many new phenomena have been observed. Among them, ^{12}Be has attracted much attention, because there is experimental evidence of the quenching of $N = 8$ shell closure [6–10].

The Be isotopes can be considered as typical examples of two-center superdeformed systems which build on an $\alpha + \alpha$ rotor of ^{8}Be. Therefore, introducing microscopic α-cluster models is quite natural for investigating the characteristic properties observed in the low-lying state of Be isotopes. Theoretical approaches based on the binary cluster picture, which assume the substructures of α and ^{6,8}He [11–13], exist. In ^{12}Be, for instance, Descouvemont and Baye have solved the coupled-channel problem between $\alpha + {}^8\mathrm{He}_{\mathrm{g.s.}}$ and its two-neutron-transfer channel, $^6\mathrm{He}_{\mathrm{g.s.}} + {}^6\mathrm{He}_{\mathrm{g.s.}}$ [13].

In the binary cluster model, stable ground nuclei as an isolated system, such as α and $^{6,8}\mathrm{He}_{\mathrm{g.s.}}$, are basically taken to be subunits in a total system. This treatment can be justified if subunits keep a large distance. If the subunits strongly overlap and interact with each other, excess neutrons cannot be localized inside one of clusters, and their orbitals spread over two core nuclei. In the case of $^{12}\mathrm{Be} = \alpha + {}^8$He, for instance, four neutrons inside ^{8}He perform the single-particle motion over two α cores when the distance of $\alpha-{}^8$He gets shorter.

The neutrons' orbits spreading over two α cores associate with the electrons' covalent bondings in molecular physics. Such covalent configurations can be described by the so-called molecular orbit (MO) method [14–16], where orbits around all the cores are constructed from the atomic orbit localized at the individual cores. In contrast to the MO method, the binary cluster state [11–13], such as $^6\mathrm{He}_{\mathrm{g.s.}} + {}^6\mathrm{He}_{\mathrm{g.s.}}$ and $\alpha + {}^8\mathrm{He}_{\mathrm{g.s.}}$ correspond to the atomic (ionic) configurations, where the electrons are trapped at one of the cores. The ionic and atomic configurations are usually handled by the valence bonding method (or Heitler-London method), where the exchanges of electrons belonging to the different cores are taken into account. Therefore, the MO states and the atomic (or ionic) ones are very different in the distributions of the neutrons' orbits; the former orbit spreads over two α cores, while the orbit is localized at one of two α cores in the latter state.

In MO configurations, a wave function of covalent neutrons is a direct product of single-particle orbitals ϕ such as $\phi(1)\phi(2)\cdots\phi(N)$ for N neutrons. Usually, a neutron's

covalent orbital ϕ is constructed by a linear combination of atomic orbital (LCAO), $\phi = \varphi_L + \varphi_R$, where φ_L (φ_R) is an atomic orbital (AO) localized at the left (right) side cores. According to LCAO treatments, whole products of MO can be expanded in terms of all the possible partitions, which are combinations of the number of the left-side AOs and right-side AOs. For example, the LCAO decomposition of the MO configuration in ^{12}Be gives the linear combination of the partitions, (^{8}He + α) + (^{7}He + ^{5}He) + (^{6}He + ^{6}He) + (^{5}He + ^{7}He) + (α + ^{8}He). In general, $^{5-8}$He are not ground states but polarized states, which contain excited states as well as a ground state. This combination can be reduced to (^{6}He + ^{6}He) + (^{5}He + ^{7}He) + (α + ^{8}He) if a projection operator on a spatial reflection is taken into account. Therefore, not only stable even-even partitions (α + ^{8}He and ^{6}He + ^{6}He) but also an odd-odd partition (^{5}He + ^{7}He), which is unstable in a limit of a complete separation of subunits, are essential in the formation of the MO configuration.

The traditional binary-cluster model, in which stable even-nuclei are set to be subunits, should be generalized so as to include the odd-odd partition to handle the MO formations and their separation into binary clusters consistently. This is the basic idea of the generalized two-center cluster model (GTCM) [17,18]. Specifically, a wave function of a total system is constructed by a superposition of all the possible AOs in two centers, and their mixing amplitudes are optimized according to variational principle. Owing to the variational optimization, the total wave function automatically generates MOs or binary states, which depend on conditions such as excitation energy, spins, and so on.

In recent studies, we have applied the GTCM to ^{12}Be and clarified the global features of the structural changes as a variation of the excitation energy [19–23]. In these studies, the low-lying states realized as bound states and the highly excited ones embedded in continuum are described in a unified manner. In the present paper, we mainly concentrate on the formation mechanism of the 0^+_1 and 0^+_2 states appearing at the bound region of ^{12}Be, although our global subject covers both the low-lying and the highly excited states. The excitation energy of the 0^+_2 state is small, about 2.24 MeV [10], and this result suggests the breaking of $N = 8$ magic number. We investigate the $N = 8$ shell quenching in ^{12}Be from the viewpoint of both the binary-cluster picture and the MO picture.

In the binary-cluster picture, we analyze an effect of ^{5}He + ^{7}He on the traditional binary-cluster treatment, such as the coupled channel of even-even clusters, (α + ^{8}He) + (^{6}He + ^{6}He). The importance of ^{5}He + ^{7}He can be speculated from the pairing interactions. When two clusters are completely separated, the energy of ^{5}He + ^{7}He is higher than that of the even-even clusters, because a pair of two valence neutrons is broken in the former. However, the pairing interactions of neutrons inside ^{5}He and ^{7}He activate when two clusters overlap. Owing to this recovered pairing, the energy of ^{5}He + ^{7}He becomes comparable to that of even-even clusters, and the coupling of even-even clusters and ^{5}He + ^{7}He becomes effective. The coupling of ^{5}He + ^{7}He to the even-even clusters is expected to reduce the neutron's kinetic energy significantly, according to the pioneering work on ^{10}Be [15].

Furthermore, GTCM makes it possible to investigate the breaking of $N = 8$ magic number in connection to the MO picture. There are two important effects on the breaking of the magic number: a formation of the $\sigma^+_{1/2}$ orbit for excess neutrons, leading to the reduction of the neutrons' kinetic energies, and the correlation energies on the $\sigma^+_{1/2}$ orbit from the triplet-odd ($\mathbf{s} = 1$) pairing, which is induced by the two-body spin-orbit interaction [15,18]. As a result of these two correlations, the energy of $(\pi^-_{3/2})^2(\sigma^+_{1/2})^2$, corresponding to $\nu(0p)^4(sd)^2$, is almost degenerate with the neutrons' closed-shell configuration. In the present study, these correlations are reanalyzed by employing the large model space beyond the previous MO model.

As shown in Refs. [19–22], the microscopic cluster model is a powerful tool for understanding the whole spectra in a nuclear system qualitatively, in which a drastic structure change from the mean-field configurations to the cluster ones appears. Thus, it should be stressed that cluster models are useful in clarifying the global features of nuclear systems. In calculations of cluster models, parameters in nucleon-nucleon (NN) interactions should be controlled so as to reproduce thresholds of cluster fragments as much as possible. Recently, the so-called "*ab initio* calculations" based on realistic NN interactions became feasible for light nuclei, and they are quite successful in reproducing the yrast states, which mainly correspond to mean-field configurations [24,25]. The treatments of cluster degrees of freedom based on current *ab initio* fashions are still in progress and are important subjects that should be handled in future studies.

In Sec. II, we give a detailed explanation of the framework of GTCM and explicit relations between the covalent MO configurations and the ionic He-cluster ones, which are useful in understanding our analysis in subsequent sections. In Secs. III A and III B, a characteristic coupling scheme in the covalent and ionic pictures are discussed by analyzing the structure of the energy surfaces, respectively. In Sec. III C, the rotational-band structures and the breaking of $N = 8$ magic number are investigated. Section IV is devoted to the summary, discussion, and future perspectives.

II. FRAMEWORK

A. Wave functions

Brief explanations on the formulation of GTCM have already been shown in Refs. [17–20]. In the present paper, we show some details of the framework of GTCM. In this method, the basis function $\{\Phi^{J^\pi K}_{\mathbf{m}}(S)\}$ is given by

$$\Phi^{J^\pi K}_{\mathbf{m}}(S) = \hat{P}^{J^\pi}_K \Phi_{\mathbf{m}}(\mathbf{S}), \tag{1}$$

$$\Phi_{\mathbf{m}}(\mathbf{S}) = \mathcal{A}\left\{\psi_L(\alpha)\psi_R(\alpha)\prod_{q=1}^{4}\varphi_q(m_q)\right\}_{\mathbf{S}}. \tag{2}$$

The α cluster $\psi_n(\alpha)$ ($n = L, R$) is expressed by the $(0s)^4$ configuration of the harmonic oscillator (HO) centered at the left (L) or right (R) side with the relative distance parameter S [26], which is explained later. The single-particle wave function for the four valence neutrons localized around one

of the α clusters is given by an AO $\varphi(j, p_k, \tau)$ with Cartesian $0p$ orbitals p_k ($k = x, y, z$) around the center j ($=L$ or R) and the nucleons' spin τ ($=\uparrow$ or $\downarrow$). In Eq. (2), $\{m_q\}$ are indices of AO (j, p_k, τ) and $\mathbf{m}$ represents a set of AOs for the four neutrons, $\mathbf{m} = (m_1, m_2, m_3, m_4)$. The constructed basis with full antisymmetrization $\mathcal{A}$ is projected to the eigenstate of the total spin J, its intrinsic angular projection K, and the total parity π by the projection operator $\hat{P}^{J^\pi}_K$.

The AO basis φ is constructed by a direct product of the $0p$ version of the Brink wave function $\phi_{jd}(\mathbf{r})$ [27], which represents a single-particle motion in the shifted HO potential with a radius $\nu = 1/2b^2$ and the nucleon's spin function $\chi_\tau(\sigma)$. The explicit expression of φ is

$$\varphi(j, p_d, \tau) \equiv \phi_{jd}(\mathbf{r})\chi_\tau(\sigma),$$
$$\phi_{jd}(\mathbf{r}) = 2\sqrt{\nu}\left(\frac{2\nu}{\pi}\right)^{3/4} \mathbf{u}_d \cdot (\mathbf{r} - \mathbf{S}_j)e^{-\nu(\mathbf{r}-\mathbf{S}_j)^2}. \quad (3)$$

In Eq. (3), $\mathbf{S}_j = (0, 0, S_j)$ with $j = L, R$ represents a shift vector of the HO's center and satisfies $\mathbf{S}_R - \mathbf{S}_L = \mathbf{S}$. A unit vector of $\mathbf{u}_d$ ($d = x, y, z$) determines the direction of the $0p$ wave function. In the shell-model limit of $\mathbf{S} \to 0$ for Eq. (2), the neutrons in the AO state with $\phi_{jd}(\mathbf{r})$ naturally occupy the higher shell except for $(0s)^4(0p_z)^4$, which are occupied by two α cores, owing to the effect of the antisymmetrizer $\mathcal{A}$ [26,27].

The total wave function is finally given by taking the superposition over S, $\mathbf{m}$, and K like

$$\hat{\Psi}^{J^\pi}_\nu = \int dS \sum_{\mathbf{m}K} C^\nu_{\mathbf{m}K}(S)\Phi^{J^\pi K}_{\mathbf{m}}(S), \quad (4)$$

and the coefficients for the νth eigenstate, $C^\nu_{\mathbf{m}K}(S)$, are determined by solving the coupled channel GCM (generator coordinate method) equation [26]. It should be stressed that S is not a dynamical coordinate but a variational parameter called the generator coordinate. By introducing the coordinate vectors for the relative motion ($\mathbf{R}$) and the center-of-mass motion ($\mathbf{R}_{\text{c.m.}}$), the basis function in Eq. (2) can be finally reduced to the following form [26]:

$$\Phi_{\mathbf{m}}(\mathbf{S}) \sim \mathcal{A}\left\{\psi_{\text{in}}(\xi_1)\psi_{\text{in}}(\xi_2)e^{-\mu\nu(\mathbf{R}-\mathbf{S})^2}e^{-A\nu\mathbf{R}^2_{\text{c.m.}}}\right\}. \quad (5)$$

Here $\psi_{\text{in}}(\xi_i)$ is an internal wave function for ith He nuclei, while the first exponential part with the reduced mass μ and the second one with the total mass A correspond to the wave functions for the relative and center-of-mass motions, respectively. The basis function $\Phi_{\mathbf{m}}(\mathbf{S})$ has a peak at $\mathbf{R} = \mathbf{S}$ and, hence, S ($=|\mathbf{S}|$) is often called the distance parameter. The basis function of $\Phi^{J^\pi}_{\mathbf{m}}(S)$ depends only on S after the operation of the projection operator of $P^{J^\pi}_K$ [26].

B. Example of LCAO treatments

In the AO basis function of Eqs. (1) and (2), excess neutrons are localized at one of the α cores. Therefore, the basis function is classified according to the partition, which is a combination of the number of the left- and right-side neutrons, and they belong to specific He-cluster states, ${}^x\text{He} + {}^y\text{He}$. However, the total wave function in Eq. (4) can describe not only the He-cluster states but also the MO structures, in which valence neutrons perform single particle motion around two α cores, because the total wave function is finally given by the superposition of the AO basis function. To see the relation between the MO and the AO more clearly, we illustrate a few examples of some MO configurations, which are important for the low-lying states in ^{12}Be.

MO configurations can be constructed by employing the so-called linear combinations of the atomic orbitals (LCAOs), $\varphi(L) \pm \varphi(R)$, where $\varphi(L)$ [$\varphi(R)$] means the left- [right-] side AO. There are three "binding orbits" which play important roles for the formation of the low-lying states. According to the LCAO treatment, the explicit expressions of these three orbits are given by

$$\pi^-_{K=+3/2} = \tilde{\varphi}(L, p_{+1}, \uparrow) + \tilde{\varphi}(R, p_{+1}, \uparrow), \quad (6)$$
$$\sigma^+_{K=+1/2} = \varphi(L, p_z, \uparrow) - \varphi(R, p_z, \uparrow), \quad (7)$$
$$\pi^-_{K=+1/2} = \tilde{\varphi}(L, p_{+1}, \downarrow) + \tilde{\varphi}(R, p_{+1}, \downarrow), \quad (8)$$

with the definition of a polar atomic orbit

$$\tilde{\varphi}(j, p_{\pm1}, \tau) = \mp\varphi(j, p_x, \tau) - i \cdot \varphi(j, p_y, \tau). \quad (9)$$

Here the relative coordinate between α cores is taken to be the z axis, which is the principal axis needed to define the K-quantum number. By taking a linear combination of the AOs defined in the Cartesian coordinate, the angular part of Eq. (9) becomes the spherical harmonics $Y_{lm}(\hat{r}_j)$ with $l = 1$, $m = \pm1$ around each α cluster ($j = L$ or R). The π^-_K orbits in Eqs. (6) and (8) have one node in the direction perpendicular to the α-α axis, while the $\sigma^+_{1/2}$ orbit has two nodes along that axis. All the AOs are labeled by good K-quantum numbers, but the π^-_K and $\sigma^+_{1/2}$ orbits become the $0p$ and $1s0d$ orbits of a naive shell model under the limit of zero α-α distance.

In a similar manner, we can construct the "antibinding orbits" by changing the signs in the linear combinations of Eqs. (6)–(8). Their expressions are given by

$$\pi^+_{K=+3/2} = \tilde{\varphi}(L, p_{+1}, \uparrow) - \tilde{\varphi}(R, p_{+1}, \uparrow), \quad (10)$$
$$\sigma^-_{K=+1/2} = \varphi(L, p_z, \uparrow) + \varphi(R, p_z, \uparrow), \quad (11)$$
$$\pi^+_{K=+1/2} = \tilde{\varphi}(L, p_{+1}, \downarrow) - \tilde{\varphi}(R, p_{+1}, \downarrow). \quad (12)$$

These three orbits have opposite parities to the respective binding orbits and have an additional node along the z axis. Thus, they correspond to the shell-model orbits with $1\hbar\omega$ excitation from the binding orbits; Eqs. (10) and (12) belong to $1s0d$ shell-model orbits, while Eq. (11) corresponds to a $1p0f$ orbit. These antibinding orbits are not main components in the low-lying 0^+ state, but the neutrons' excitations to the antibinding orbits give important correlation energies.

From the binding orbits, we can construct the MO configurations of the valence four neutrons, which are dominant in the low-lying 0^+ states in ^{12}Be. First, we show the expression of $(\pi^-_{3/2})^2(\sigma^+_{1/2})^2$, corresponding to the $\nu(0p)^4(1s0d)^2$ configuration at the zero limit of the α-α distance. This configuration is the most important for the ground state, and its explicit form of the wave function is written as

follows:

$$\begin{aligned}\hat{\Phi}^{+K=0}(S) &= \mathcal{A}\{\pi^-_{+3/2}\pi^-_{-3/2}\sigma^+_{+1/2}\sigma^+_{-1/2}\}\\ &= \hat{Q}^{(+)}\mathcal{A}\{\tilde{\varphi}(L,p_{+1},\uparrow)\tilde{\varphi}(L,p_{-1},\downarrow)\varphi(L,p_z,\uparrow)\varphi(L,p_z,\downarrow)\\ &\quad+\tilde{\varphi}(L,p_{+1},\uparrow)\tilde{\varphi}(L,p_{-1},\downarrow)\cdot\varphi(R,p_z,\uparrow)\varphi(R,p_z,\downarrow)+\tilde{\varphi}(L,p_{+1},\uparrow)\varphi(L,p_z,\uparrow)\cdot\tilde{\varphi}(R,p_{-1},\downarrow)\varphi(R,p_z,\downarrow)\\ &\quad-\tilde{\varphi}(L,p_{+1},\uparrow)\varphi(L,p_z,\downarrow)\cdot\tilde{\varphi}(R,p_{-1},\downarrow)\varphi(R,p_z,\uparrow)-2\tilde{\varphi}(L,p_{+1},\uparrow)\tilde{\varphi}(L,p_{-1},\downarrow)\varphi(L,p_z,\uparrow)\cdot\varphi(R,p_z,\downarrow)\\ &\quad-2\tilde{\varphi}(L,p_{+1},\uparrow)\varphi(L,p_z,\uparrow)\varphi(L,p_z,\downarrow)\cdot\tilde{\varphi}(R,p_{-1},\downarrow)\}. \end{aligned} \tag{13}$$

In this expression, the wave function of two α particles $\psi_L(\alpha)\psi_R(\alpha)$ is omitted for simplicity, and $\hat{Q}^{(+)}$ is an operator which has the form of

$$\hat{Q}^{(+)} = (1+e^{-iJ_y\pi})\mathcal{P}^{(+)}, \tag{14}$$

where J_y and $\mathcal{P}^{(+)}$ are the rotation operator with respect to the Y axis [28] and the projection operator to the positive parity state, respectively. In a naive expansion of Eq. (13), another AO basis, which are constructed by an exchange of $L \leftrightarrow R$, such as $LLLL \rightarrow RRRR$ for instance, appears in addition to the terms in Eq. (13), but we need to consider only one of the combinations by introducing the $\hat{Q}^{(+)}$ operator. Thus, in the present study, we consider only one combination of (L, R), as shown in Eq. (13). The operation of $\hat{Q}^{(+)}$ can be completely achieved when the angular momentum projection is performed exactly.

Equation (13) shows that the wave function with the $(\pi^-_{3/2})^2(\sigma^+_{1/2})^2$ configuration can be decomposed into the AO basis such as $^8\mathrm{He}+\alpha(LLLL)$, $^6\mathrm{He}+{}^6\mathrm{He}(LL\cdot RR)$, and $^7\mathrm{He}+{}^5\mathrm{He}(LLL\cdot R)$. Therefore, the coherent mixing of possible partitions occurs in the MO states.

Next, we show another example of the MO configuration of $(\pi^-_{3/2})^2(\pi^-_{1/2})^2$. This configuration smoothly changes into the neutron's closed-shell configuration of $\nu(0p)^6$ in the shell-model limit of zero α-α distance ($S=0$). The expression of this MO configuration in terms of the AO basis is given by

$$\begin{aligned}&\hat{\Phi}^{+K=0}(S)\\ &= \mathcal{A}\{\pi^-_{+3/2}\pi^-_{-3/2}\pi^-_{+1/2}\pi^-_{-1/2}\}\\ &= \hat{Q}^{(+)}\mathcal{A}\{\tilde{\varphi}(L,p_{+1},\uparrow)\tilde{\varphi}(L,p_{-1},\downarrow)\tilde{\varphi}(L,p_{+1},\uparrow)\tilde{\varphi}(L,p_{+1},\downarrow)+\tilde{\varphi}(L,p_{+1},\uparrow)\tilde{\varphi}(L,p_{-1},\downarrow)\cdot\tilde{\varphi}(R,p_{+1},\downarrow)\tilde{\varphi}(R,p_{-1},\uparrow)\\ &\quad-\tilde{\varphi}(L,p_{+1},\uparrow)\tilde{\varphi}(L,p_{+1},\downarrow)\cdot\tilde{\varphi}(R,p_{-1},\downarrow)\tilde{\varphi}(R,p_{-1},\uparrow)-\tilde{\varphi}(L,p_{+1},\uparrow)\tilde{\varphi}(L,p_{-1},\uparrow)\cdot\tilde{\varphi}(R,p_{-1},\downarrow)\tilde{\varphi}(R,p_{+1},\downarrow)\\ &\quad+\tilde{\varphi}(L,p_{+1},\uparrow)\tilde{\varphi}(L,p_{-1},\downarrow)\tilde{\varphi}(L,p_{+1},\downarrow)\cdot\tilde{\varphi}(R,p_{-1},\uparrow)+\tilde{\varphi}(L,p_{+1},\uparrow)\tilde{\varphi}(L,p_{+1},\downarrow)\tilde{\varphi}(L,p_{-1},\uparrow)\cdot\tilde{\varphi}(R,p_{-1},\downarrow)\}. \end{aligned} \tag{15}$$

The $S=0$ limit of the simple binary clusters, $^8\mathrm{He}_{\mathrm{g.s.}}+\alpha$, $^6\mathrm{He}_{\mathrm{g.s.}}+{}^6\mathrm{He}_{\mathrm{g.s.}}$, and $^7\mathrm{He}_{\mathrm{g.s.}}+{}^5\mathrm{He}_{\mathrm{g.s.}}$, has a large overlap with the shell-model state of $\nu(0p)^6$, but all the partitions must be coherently mixed to form the $(\pi^-_{3/2})^2(\pi^-_{1/2})^2$ configuration at finite S.

In Eqs. (13) and (15), the mixing amplitudes of the AO basis are uniquely determined according to LCAO approximation. However, they can be optimized by diagonalizing the total Hamiltonian with the AO basis. In the present analysis, therefore, we optimized the mixing amplitudes of the AO basis by calculating the energy of a given MO configuration. As a result of this optimization, the amplitudes deviate from those in ideal MOs shown in Eqs. (13) and (15), but this deviation is not so large for low-lying states with MO structure.

We also illustrate that the basis functions of Eq. (2) can describe the cluster-model states in which neutrons' orbits have definite spin around one of the α cores. For example, the $^8\mathrm{He}+\alpha$ configuration, in which the valence neutron forms 0^+ with $(0p_{3/2})^4$ around one of the α clusters can be constructed as follows:

$$\Phi^{K=0}(S) = \mathcal{A}\left\{\psi_L(\alpha)\psi_R(\alpha)\phi_L^{+3/2}\phi_L^{-3/2}\phi_L^{+1/2}\phi_L^{-1/2}\right\}. \tag{16}$$

Here the $0p_{3/2}$ orbit in the jj-coupling scheme, ϕ^{j_z} with j_z component is given by

$$\phi_L^{+3/2} = \tilde{\varphi}(L,p_{+1},\uparrow), \tag{17}$$

$$\phi_L^{-3/2} = \tilde{\varphi}(L,p_{-1},\downarrow), \tag{18}$$

$$\phi_L^{+1/2} = \frac{1}{\sqrt{3}}\tilde{\varphi}(L,p_{+1},\downarrow)+\sqrt{\frac{2}{3}}\varphi(L,p_z,\uparrow), \tag{19}$$

$$\phi_L^{-1/2} = \frac{1}{\sqrt{3}}\tilde{\varphi}(L,p_{-1},\uparrow)+\sqrt{\frac{2}{3}}\varphi(L,p_z,\downarrow), \tag{20}$$

where the mixing amplitudes are determined by the Clebsh-Gordon coefficients. Therefore, the basis function of Eq. (2) can describe the combinations of the asymptotic cluster structures as well as the MO ones.

Because the ground and low-lying bands are mainly investigated in the present study, the present basis is restricted to the axially symmetric ($K = 0$) configurations. However, we include all the possible AO configurations for the four valence neutrons within this approximation. Therefore, the model space of MO, where each valence neutron rotates around two centers simultaneously, and that of binary clusters, where neutrons are localized around one of an α core, are covered [17]. The number of the employed AO basis $\Phi^{J^\pi K=0}_{\mathbf{m}}$ is 38, and all these bases can transform to the MO states or the cluster-model ones using expressions similar to Eqs. (13), (15), and (16).

C. Hamiltonian and adiabatic treatments

The total Hamiltonian $\hat{H}$ employed in the present calculation is

$$\hat{H} = \sum_{i}^{12} \hat{t}_i - \hat{T}_{\text{c.m.}} + \sum_{i<j}^{12} \hat{v}^{(\text{C})}_{ij} + \sum_{i<j}^{12} \hat{v}^{(\text{LS})}_{ij}, \tag{21}$$

where i and j denote a number of nucleons. $\hat{t}$ represents a single nucleon's kinetic energy, while $\hat{v}^{(\text{C})}_{ij}$ and $\hat{v}^{(\text{LS})}_{ij}$ are the two-body nucleon-nucleon (NN) interactions for the central and spin-orbit parts, respectively. The kinetic energy of the center-of-mass (c.m.) motion, shown by $\hat{T}_{\text{c.m.}}$, is subtracted from the summation of the nucleon's kinetic energy. In the present treatment, the c.m. motion of the total system can be exactly eliminated.

As for the NN interaction, we use the Volkov No. 2 [29] and the G3RS [30] for the central $\hat{v}^{(\text{C})}_{ij}$ and spin-orbit $\hat{v}^{(\text{LS})}_{ij}$ parts, respectively. The functional form of the NN interactions are

$$\hat{v}^{(\text{C})}_{ij} = v^{(\text{C})}(r_{ij})(W - MP_\sigma P_\tau + BP_\sigma - HP_\tau), \tag{22}$$

$$\hat{v}^{(\text{LS})}_{ij} = v^{(\text{LS})}(r_{ij})P(^3O)\mathbf{L}_{ij} \cdot \mathbf{S}_{ij}. \tag{23}$$

In the central interaction, W, $MP_\sigma P_\tau$, BP_σ, and HP_τ denote the Wigner, Majorana, Bartlett, and Heisenberg exchanges, while, in the spin-orbit interaction, $P(^3O)$ represents the projection operator on the triplet-odd state. $\mathbf{L} = \hat{\mathbf{r}}_{ij} \times \hat{\mathbf{p}}_{ij}$ and $\mathbf{S} = \mathbf{s}_i + \mathbf{s}_j$ are the relative and total nucleons' spins for interacting ith and jth nucleons, respectively.

The parameters in the interactions and the b parameter of HO are the same as those applied in Refs. [18,19], which successfully reproduced the properties of ^{10}Be. The adopted parameters are shown in the caption of Table I. In Table I, the calculated thresholds for the lowest four open channels are shown. The energy difference of $\alpha + {}^8\text{He}_{\text{g.s.}}$ and ${}^6\text{He}_{\text{g.s.}} + {}^6\text{He}_{\text{g.s.}}$ in the calculation is a little larger than that in the experimental observation, but the relative differences among the thresholds are reasonably reproduced by the present NN interaction.

Because the threshold energy corresponds to the order of magnitude of the interaction strength to dissociate a compound system into a pair of clusters, the reproduction of the threshold energy is crucial in discussing the appearance and disappearance of the cluster degrees of freedom. Therefore, optimizing the NN force adopted to give correct threshold energies of possible cluster configurations as much as possible is important.

TABLE I. Comparisons of the threshold energies in the calculation with those in the experiment. All the energies are measured from the energy of the calculated ground state (units of MeV). The parameters of Volkov No. 2 are $M = 0.643$ and $B = H = 0.125$, while the strength of G3RS is taken to be $+3000$ and -2000 MeV for the repulsive and attractive parts, respectively. The radius parameter of HO b is fixed to 1.46 fm.

Channel	Experiment	Calculation
$\alpha + {}^8\text{He}_{\text{g.s.}}$	9.0	9.3
${}^6\text{He}_{\text{g.s.}} + {}^6\text{He}_{\text{g.s.}}$	10.1	11.8
${}^6\text{He}_{\text{g.s.}} + {}^6\text{He}(2^+_1)$	11.9	13.7
${}^5\text{He}_{\text{g.s.}} + {}^7\text{He}_{\text{g.s.}}$	13.2	14.6

If we fix the distance parameter S for the α-α core and diagonalize the Hamiltonian shown in Eq. (21), we obtain the energy eigenvalues for a given S. Namely, we solve

$$\left[\hat{H} - E^{J^\pi}_\mu(S)\right]\Phi^{J^\pi\mu}_{\text{AS}}(S) = 0, \tag{24}$$

$$\Phi^{J^\pi\mu}_{\text{AS}}(S) = \sum_{\mathbf{m}K} D^{J^\pi\mu}_{\mathbf{m}K}(S)\Phi^{J^\pi\mu}_{\mathbf{m}K}(S). \tag{25}$$

The μth eigenvalue $E^{J^\pi}_\mu(S)$ is a function of the relative distance-parameter S, and a sequence of $E^{J^\pi}_\mu(S)$ forms the energy surfaces. The energies $E^{J^\pi}_\mu(S)$ and wave functions $\Phi^{J^\pi\mu}_{\text{AS}}(S)$ correspond to the so-called "adiabatic energy surfaces (AESs)" and "adiabatic states (ASs)," respectively, in atomic physics. In this report, we call the calculation including all the possible AO bases labeled by $\mathbf{m}$ in Eq. (4) the complete (full) GTCM calculation in the adiabatic treatment.

III. RESULTS

A. Analysis based on the MO picture

We obtained two 0^+ states (0^+_1, 0^+_2) in a bound region by solving the eigenvalue problem with the total wave function in Eq. (4). The excitation energy of 0^+_2 is about 2.12 MeV, which nicely reproduces the recent observation (2.24 MeV) [10], and we mainly analyze the formation mechanism of these two states with a close energy spacing. In this section, we investigate the structures of energy surfaces of the MO states, $(\pi^-_{3/2})^2(\sigma^+_{1/2})^2$ and $(\pi^-_{3/2})^2(\pi^-_{1/2})^2$, which are dominant configurations for the 0^+_1 and 0^+_2 states, respectively, to clarify the mechanism of the breaking of the $N = 8$ magic number in ^{12}Be. In Sec. III A1, we analyze an energy competition between $(\pi^-_{3/2})^2(\sigma^+_{1/2})^2$ and $(\pi^-_{3/2})^2(\pi^-_{1/2})^2$. There is a large correlation energy for the former MO induced by the neutrons' triplet odd pairing. The solutions of the coupled-channel calculation of $(\pi^-_{3/2})^2(\sigma^+_{1/2})^2$ with correlation and $(\pi^-_{3/2})^2(\pi^-_{1/2})^2$ are shown in Sec. III A2. In Sec. III A3, the comparison of the MO calculation with the complete GTCM calculation is discussed.

1. Correlation energies for the MO states

We calculate energy surfaces of $(\pi^-_{3/2})^2(\sigma^+_{1/2})^2$ and $(\pi^-_{3/2})^2(\pi^-_{1/2})^2$ by solving the eigenvalue problem with the AO basis included in Eqs. (13) and (15), respectively, and hence, the mixing amplitudes of the AOs in each MO configuration are optimized. The former and latter configurations correspond to the $\nu(0p)^4(1s0d)^2$ and closed-shell configurations, respectively, at the limit of $S = 0$. In Fig. 1, the (1) shows the result of the pure $(\pi^-_{3/2})^2(\pi^-_{1/2})^2$, while the energy of the pure $(\pi^-_{3/2})^2(\sigma^+_{1/2})^2$ is shown by curve (A).

On the surface of $(\pi^-_{3/2})^2(\sigma^+_{1/2})^2$ (A), a broad minimum around $S \sim 4$ fm appears, which is more clusterized than that of $(\pi^-_{3/2})^2(\pi^-_{1/2})^2$ [$S \sim 3$ fm in curve (1)]. Therefore, the prolate deformation is much enhanced in the former configuration [14,15,17,18]. This is because the $\sigma^+_{1/2}$ orbit with an enlarged distribution along the α-α axis enhances the α clustering so as to reduce the neutrons' kinetic energy. However, in this naive MO model, the energy minimum of $(\pi^-_{3/2})^2(\sigma^+_{1/2})^2$ is much higher than that of $(\pi^-_{3/2})^2(\pi^-_{1/2})^2$ (1) and, hence, $N = 8$ is considered a good magic number.

We consider a correlation on $(\pi^-_{3/2})^2(\sigma^+_{1/2})^2$ based on naive particle-hole excitation. In the $K^\pi = 0^+$ state, the 1p-1h excitation of $(\sigma^+_{1/2})^2 \to (\sigma^+_{1/2}\pi^+_{1/2})$ gives an important correlation energy because both $\sigma^+_{1/2}$ and $\pi^+_{1/2}$ shown in Eqs. (7) and (12) belong to the $1s0d$ shells in a naive shell-model limit with $S = 0$. There is a similar 1p-1h excitation of $(\sigma^+_{1/2})^2 \to (\sigma^+_{1/2}\pi^+_{3/2})$, but this coupling has no effects in the $J^\pi = K^\pi = 0^+$ calculation because $(\sigma^+_{1/2}\pi^+_{3/2})$ has a nonzero K number, $|K| \geqslant 1$. $(\sigma^+_{1/2}\pi^+_{1/2})$ has the spin-triplet ($\mathbf{s} = 1$) configuration, while two neutrons form the spin-singlet ($\mathbf{s} = 0$) configuration in $(\sigma^+_{1/2})^2$. This means that the coupling of these two MO configurations is mainly induced by the two-body spin-orbit interaction. The coupling scheme in a shell-model picture is explained in the following.

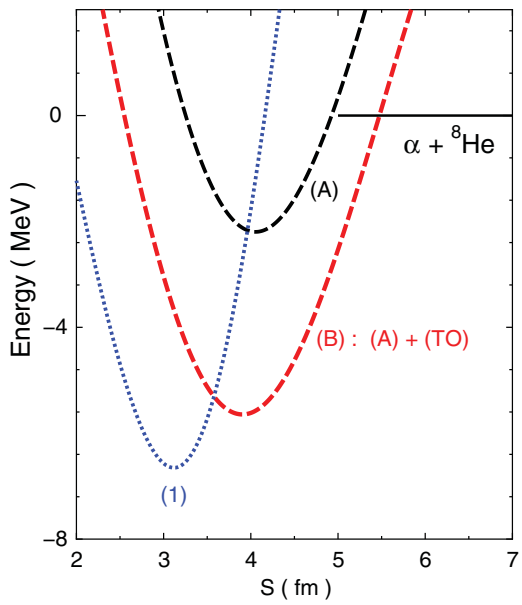

FIG. 1. (Color online) Energy shift for the σ^+ orbital ($J^\pi = 0^+$). Curve (A) represents the energy of the pure $(\pi^-_{3/2})^2(\sigma^+_{1/2})^2$ without any correlations, while the (B) shows the energy curve of $(\pi^-_{3/2})^2(\sigma^+_{1/2})^2$ with a correlation of the $\mathbf{s} = 1$ configuration, $(\pi^-_{3/2})^2(\sigma^+_{1/2}\pi^+_{1/2})$. Curve (1) shows the surface of the pure $(\pi^-_{3/2})^2(\pi^-_{1/2})^2$. See text for details.

In a naive LS-coupling scheme, the $\mathbf{s} = 0$ and $\mathbf{s} = 1$ states are mainly constructed by the $1s0d$-shell orbits such as

$$|\mathbf{s} = 0, (\sigma^+_{1/2})^2\rangle \sim C(S)|[S \otimes S]_0 \otimes [1/2 \otimes 1/2]_0\rangle_{J=0} + C(D)|[D \otimes D]_0 \otimes [1/2 \otimes 1/2]_0\rangle_{J=0} \quad (26)$$

and

$$|\mathbf{s} = 1, (\pi^+_{1/2}\sigma^+_{1/2})\rangle \sim |[D \otimes D]_1 \otimes [1/2 \otimes 1/2]_1\rangle_{J=0}. \quad (27)$$

Here the ket states denote the two nucleons' single-particle state with the LS-coupling scheme, $|[l_1 \otimes l_2]_l \otimes [s_1 \otimes s_2]_\Lambda\rangle$, in which l_i and s_i represent the orbital and nucleon spin for the ith neutron ($i = 1,2$). The symbols of l and Λ denote the total spatial and intrinsic spins, and they are totally coupled to $J = 0$ in both the $\mathbf{s} = 0$ and the $\mathbf{s} = 1$ states.

The $\mathbf{s} = 0$ state in Eq. (26) includes both a component of $[S \otimes S]_0$ and $[D \otimes D]_0$ with the amplitude of $C(S)$ and $C(D)$, respectively. This is because the σ^+ orbital contains mainly components of the S-wave and D-wave orbitals. However, the $\mathbf{s} = 1$ state is mainly constructed by the D-wave component, $[D \otimes D]$, because of the angular momentum coupling. Although the $\mathbf{s} = 0$ state in Eq. (26) contains the two components of $[S \otimes S]$ and $[D \otimes D]$, the latter component mainly contributes to the matrix element of the two-body spin-orbit force, $\langle \mathbf{s} = 1|\hat{v}^{(\mathrm{LS})}|\mathbf{s} = 0\rangle$, owing to the similarity of the radial shape of the wave functions in the bra and ket states. Therefore, the coupling of the two neutrons in $(\sigma^+_{1/2})^2$ ($\mathbf{s} = 0$) to $(\sigma^+_{1/2}\pi^+_{1/2})$ ($\mathbf{s} = 1$) just corresponds to a kind of pairing correlation in the D-wave state.

In this paper, we call the coupling to $\mathbf{s} = 1$ the "spin-triplet pairing." The spin-triplet state corresponds to the triplet-odd (TO) state, in which two neutrons move with odd relative spin. The spin-triplet pairing is a characteristic coupling scheme, appearing in the σ^+ orbital configuration. The effect is quite large, because the σ^+ orbital contains the D-wave component.

The binding energy gain generated by the spin-triplet pairing can be confirmed in Fig. 1. Curve (B) includes the spin-triplet (TO) pairing correlation [(A) + TO]. Here, we include all of the AO configurations needed to form $(\pi^-_{3/2})^2(\sigma^+_{1/2}\pi^+_{1/2})$ and take into account the spin-triplet pairing correlation as much as possible. By comparing (A) with (B), we can see the large energy gain (∼4 MeV) owing to the coupling to the $\mathbf{s} = 1$ configuration. As a result of this energy gain, the local minimum of (B) comes close to that of $(\pi^-_{3/2})^2(\pi^-_{1/2})^2$ as shown by curve (1). This is consistent with the result shown in Refs. [15,18]. Thus, $(\pi^-_{3/2})^2(\sigma^+_{1/2})^2$ can be considered as the intruder state.

The importance of the TO pairing effect can also be confirmed in the decomposition of the total energy into kinetic energy $\langle T\rangle$, central potential $\langle V_c\rangle$, and spin-orbit one $\langle V_{\mathrm{LS}}\rangle$. Table II shows the decomposition of the energy surface (A) and (B) in Fig. 1 around the local minimum point of $S = 3.6$ fm, which is common distance for both (A) and (B). $\langle V_{\mathrm{LS}}\rangle$ is enhanced in (B) with the TO pairing in comparison to (A)

TABLE II. The expectation values of kinetic energy $\langle T\rangle$, central interaction $\langle V_c\rangle$, and LS interaction $\langle V_{LS}\rangle$ around the minimum point of $S = 3.6$ fm. The contribution from the Coulomb interaction is included in $\langle V_c\rangle$. (A) and (B) in this table represent the energy decomposition of the surface (A) and (B) at $S = 3.6$ fm (Fig. 1), respectively. All the values are shown in units of MeV.

Surface	$\langle T\rangle$	$\langle V_c\rangle$	$\langle V_{LS}\rangle$
(A)	200.49	−227.90	−8.02
(B)	200.72	−226.53	−13.47

without the TO pairing, while the other two parts, $\langle T\rangle$ and $\langle V_c\rangle$, are almost constants in the results with and without the TO pairing.

On the contrary, a candidate of a correlation on $(\pi^-_{3/2})^2(\pi^-_{1/2})^2$ is the coupling of $(\pi^-_{1/2})^2 \to (\pi^+_{3/2})^2$ in the $K^\pi = 0^+$ state. The former and latter configurations correspond to $(0p)^2$ and $(1s0d)^2$, respectively, in a spherical shell model. Therefore, this coupling corresponds to the pairing excitation from the $0p$ shell to the $1s0d$ shell. We included the pairing excitation for $(\pi^-_{3/2})^2(\pi^-_{1/2})^2$ and found that energy gain (ΔE) owing to the pairing excitation of $(\pi^-_{1/2})^2 \to (\pi^+_{3/2})^2$ is quite small, $\Delta E < 100$ keV, around the local minimum point. Therefore, the correlation energy for $(\pi^-_{3/2})^2(\pi^-_{1/2})^2$ can be negligible. This is because the pairing excitation requires the $2\hbar\omega$ jump across the major shell. Around the local minimum point ($S \sim 3.2$ fm), the shell gap between the $0p$ shell and the $1s0d$ shell is large, and this large gap leads to the minor contribution of the second-order perturbation from the pairing excitation.

We call the MO solutions [curve (B) in Fig. 1] including the TO correlations "the correlated MO," which is denoted by the double quotation mark ("MO"). As a result of the correlations, the minimum energy of $(\pi^-_{3/2})^2(\pi^-_{1/2})^2$ [$\nu(0p)^6$ in the $S = 0$ limit] becomes comparable to "$(\pi^-_{3/2})^2(\sigma^+_{1/2})^2$" [$\nu(0p)^4(1s0d)^2$].

2. Solutions of "$(\pi^-_{3/2})^2(\sigma^+_{1/2})^2$" + $(\pi^-_{3/2})^2(\pi^-_{1/2})^2$

We investigate the coupling of the correlated "$(\pi^-_{3/2})^2(\sigma^+_{1/2})^2$" and $(\pi^-_{3/2})^2(\pi^-_{1/2})^2$ in Fig. 2. In this figure, the energy of the correlated "$(\pi^-_{3/2})^2(\sigma^+_{1/2})^2$" [curve (B)] and the pure $(\pi^-_{3/2})^2(\pi^-_{1/2})^2$ [curve (1)] are shown.

As shown in Fig. 2, a crossing point around $S = 3.6$ fm appears in the surfaces of (B) and (1) owing to the energy gain of the former configuration. In this figure, the black curves represent the solutions of the coupled channel calculations of (1) + (B), which is equivalent to the calculation of $(\pi^-_{3/2})^2(\pi^-_{1/2})^2 + (\pi^-_{3/2})^2(\sigma^+_{1/2})^2 + (\pi^-_{3/2})^2(\pi^+_{1/2}\sigma^+_{1/2})_{s=1}$. Here we include all the AO bases, which are needed to construct these three configurations. We can see the large energy splitting around the crossing point. Owing to the close energy of (B) and (1), the "$(\pi^-_{3/2})^2(\sigma^+_{1/2})^2$" and $(\pi^-_{3/2})^2(\pi^-_{1/2})^2$ configurations are strongly mixed with each other around the crossing point. In a naive shell-model picture, therefore, the $\nu(0p)^6$ and $\nu(0p)^4(1s0d)^2$ configurations coexist around the crossing point of $S \sim 3.6$ fm. The former configuration is dominant in the region of $S \leqslant 3.6$ fm, while the dominant configuration is replaced by the latter state outside of the crossing point, $S \geqslant 3.6$ fm.

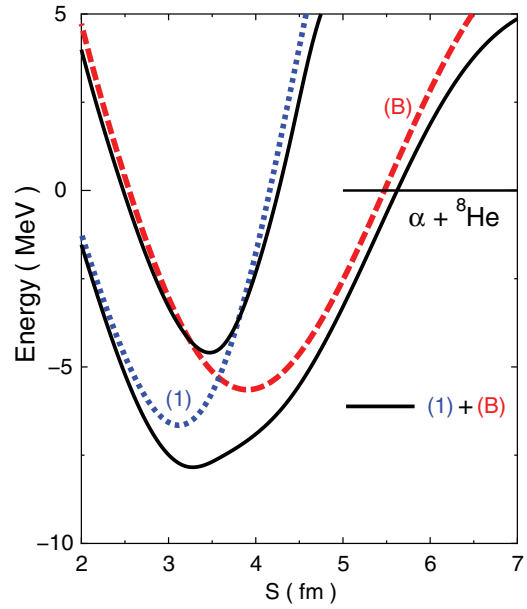

FIG. 2. (Color online) Energy surfaces of the correlated MO configurations ($J^\pi = 0^+$). Curve (B) represents the correlated "$(\pi^-_{3/2})^2(\sigma^+_{1/2})^2$" configuration with $\mathbf{s} = 1$, while curve (1) shows the pure $(\pi^-_{3/2})^2(\pi^-_{1/2})^2$ configuration. The solid curves show the result of the coupled channels of (1) and (B).

3. Comparison of the MO picture with GTCM

The coupled-channel calculation of the correlated "MOs" almost reproduces AESs as shown in Fig. 3. Here the complete GTCM result is obtained by the coupled-channel calculation of the 38 AO bases, while, in the the calculation of the correlated MOs, the 23 AO bases are included. The energies of the correlated MOs (solid curves) are almost the same as those of the AESs with the complete basis (dotted curves). The energy difference between the former and the latter is only about 0.44 and 0.95 MeV at the local minimum points for the lowest and second surfaces, respectively. This result means that the behaviors of the AESs in the full calculation can be well understood by the coupling between the correlated "$(\pi^-_{3/2})^2(\sigma^+_{1/2})^2$" and $(\pi^-_{3/2})^2(\pi^-_{1/2})^2$, and the MO bases nicely work to describe the low-lying 0^+ states. GTCM covers the model space beyond that of the MO picture, but the low-lying states are almost converged in the MO space.

The individual contributions of the kinetic and potential energies to the lowest minimum are shown in Table III. In the naive MO picture without any correlation, the energy of $(\pi^-_{3/2})^2(\pi^-_{3/2})^2$ denoted by (1) is the lowest around $S \sim 3.2$ fm. In this configuration, the contribution from the spin-orbit interaction $\langle V_{LS}\rangle$ is quite small owing to the cancellation of the spin-orbit parallel $[(\pi^-_{3/2})^2]$ and antiparallel $[(\pi^-_{1/2})^2]$ contributions. In the full GTCM calculation at the same S, the $\mathbf{s} = 1$ TO paired configuration is strongly mixed through the coupling

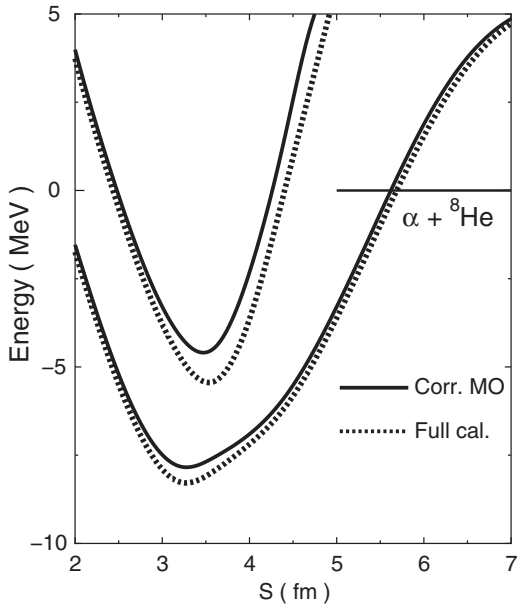

FIG. 3. The comparison of the AESs obtained by the full model space with those obtained by the correlated MO configurations ($J^\pi = 0^+$). The dotted and solid curves represent the solutions of the full calculations and those of the correlated MO, respectively.

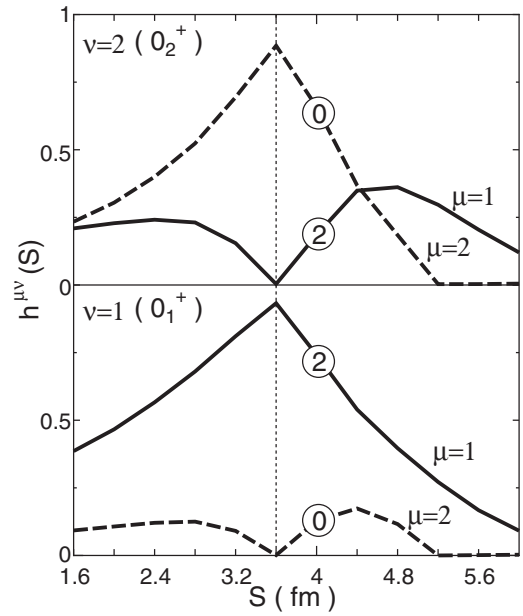

FIG. 4. Squared overlap of the ASs [$\Phi^\mu_{\rm AS}(S)$, $\mu = 1, 2$] and the full solutions (Ψ^ν, $\nu = 1, 2$). The bottom and top panels show the result for $\nu = 1$ (0^+_1) and $\nu = 2$ (0^+_2), respectively. The distribution of the ASs are shown by the solid curve ($\mu = 1$) and the dashed one ($\mu = 2$). The dotted lines represent the crossing point of the correlated MO state, (1) and (B), shown in Fig. 2. The ⓪ and ② denote the dominance of $0\hbar\omega$ and $2\hbar\omega$, respectively. See text for details.

of $(\pi^-_{3/2})^2(\pi^-_{1/2})^2 + (\pi^-_{3/2})^2(\sigma^+_{1/2})^2 + (\pi^-_{3/2})^2(\pi^+_{1/2}\sigma^+_{1/2})_{s=1}$. This mixture leads to the enhancement of the contribution of $\langle V_{\rm LS}\rangle$. Because the correlated "$(\pi^-_{3/2})^2(\sigma^+_{1/2})^2$" becomes dominant at the outer region of the crossing point ($S \geqslant 3.6$ fm), which is shown in Fig. 2, the magnitude of $\langle V_{\rm LS}\rangle$ increases further in the outer region of $S \geqslant 3.6$ fm.

Energy levels are calculated by solving the eigenvalue equation with the total wave function in Eq. (4), where the distance parameter S is superposed. In this method, we set a range of S to be 1.2–6.8 fm with a mesh of $\Delta S = 0.4$ fm. To investigate the intrinsic structure of the $0^+_{1,2}$ states, we calculate the squared overlap of the energy levels and the lowest two adiabatic states, which have dominant components of the pure $(\pi^-_{3/2})^2(\sigma^+_{1/2})^2$ and $(\pi^-_{3/2})^2(\pi^-_{1/2})^2$ configurations. The squared overlap of the μth AS, $\Phi^\mu_{\rm AS}(S)$, and the νth energy level, Ψ^ν, are

$$h^{\mu\nu}(S) = \left|\left\langle \Phi^\mu_{\rm AS}(S)\middle|\Psi^\nu\right\rangle\right|^2, \quad \mu = 1, 2, \nu = 1, 2. \tag{28}$$

Here $\mu = 1$ and $\mu = 2$ represent the lowest and second ASs, respectively, while $\nu = 1$ and $\nu = 2$ correspond to the energy level of 0^+_1 and 0^+_2, respectively. In Fig. 4, the distribution of the ASs of $\mu = 1$ (solid curves) and $\mu = 2$ (dashed curves) are shown in both the 0^+_1 ($\nu = 1$) and 0^+_2 ($\nu = 2$) states. The $\mu = 1, 2$ ASs are dominantly contained in these two energy levels.

From this figure, we understand that the distributions of the squared overlap spread over a wide region of S. There are deep minima in the AESs shown in Fig. 3 ($S_{\rm min} = 3.2$ fm for the $\mu = 1$ AES and $S_{\rm min} = 3.6$ fm for the $\mu = 2$ AES) but the amplitudes of the ASs are not localized at the minimum point and have long-range tails. This means that, in superposing the distance parameter S, the zero point oscillation appears in the α-α relative motion, and it is possible to mix other configurations beyond the optimal distance S. Thus, a single AS at a local minimum point cannot necessarily describe a total system.

The 0^+_1 state has a large amplitude of the $\mu = 1$ ASs in the whole distance region; hence, the $\mu = 1$ AS mainly generates the 0^+_1 state. In these distributions, the amplitude of the outside region is important to characterize the intrinsic structure because, at the inner region, a strong mixing of ASs occurs owing to the antisymmetrization effect, which makes it difficult to interpret the intrinsic structure. Owing to this difficulty, we focus on the amplitude outside the crossing point ($S = 3.6$ fm) of AES (1) and (B). As can be confirmed in Fig. 2,

TABLE III. The expectation values of kinetic energy $\langle T\rangle$, central interaction $\langle V_{\rm c}\rangle$, and LS interaction $\langle V_{\rm LS}\rangle$ around the minimum point. (1) represents the pure MO configuration of $(\pi^-_{3/2})^2(\pi^-_{1/2})^2$ shown in Fig. 1, while GTCM represents the result of the lowest energy surface in the complete GTCM calculation. The S means the distance parameter, at which the energy is calculated. All the values are shown in units of MeV.

Surface	S	$\langle T\rangle$	$\langle V_{\rm c}\rangle$	$\langle V_{\rm LS}\rangle$
(1)	3.2	191.59	−232.13	-5.06×10^{-3}
GTCM	3.2	193.98	−232.55	−3.62
GTCM	3.6	191.89	−226.13	−7.60
GTCM	4.0	191.92	−221.04	−12.00
GTCM	4.8	185.12	−211.65	−11.97

in the outside region beyond the crossing point, the $\mu = 1$ AS has the main component of $(\pi^-_{3/2})^2(\sigma^+_{1/2})^2$. In the limit of $S = 0$, this MO configuration corresponds to $\nu(0p)^4(1s0d)^2$ with the $2\hbar\omega$ jump from the closed-shell configuration, $\nu(0p)^6$. Thus, we call $(\pi^-_{3/2})^2(\sigma^+_{1/2})^2$ the $2\hbar\omega$ state, while $(\pi^-_{3/2})^2(\pi^-_{1/2})^2$, which has a large amplitude of $\nu(0p)^6$, is expressed by the $0\hbar\omega$ state. In Fig. 4, the crossing point is shown by the dotted lines, and the dominance of $2\hbar\omega$ ($0\hbar\omega$) is denoted by the symbol of ② (⓪) on the solid (dashed) curve. We can clearly understand the dominance of the $2\hbar\omega$ configuration in the 0^+_1 state.

The dominance of the $(\pi^-_{3/2})^2(\sigma^+_{1/2})^2$ in the 0^+_1 energy level can be attributed to the two-body spin-orbit interaction $\hat{v}^{(\mathrm{LS})}$. Because the energy minimum of the $0\hbar\omega$ MO, $(\pi^-_{3/2})^2(\pi^-_{1/2})^2$, is slightly deeper than that of $2\hbar\omega$ MO, $(\pi^-_{3/2})^2(\sigma^+_{1/2})^2$, the 0^+_1 state produced from the local minimum region of the surface (1) + (B) in Fig. 2 should have about 50% (or a little larger) component of the $0\hbar\omega$ MO and 50% (or a little smaller) component of the $2\hbar\omega$ MO. Such an equal mixture actually happens at the crossing point of (1) and (B), $S = 3.6$ fm. However, the large matrix element of the spin-triplet pairing, $\langle(\sigma^+_{1/2})^2|\hat{v}^{(\mathrm{LS})}|(\sigma^+_{1/2}\pi^+_{1/2})\rangle$, induces the strong coupling among the different S, such as $(\pi^-_{3/2})^2(\sigma^+_{1/2})^2S \leftrightarrow (\pi^-_{3/2})^2(\sigma^+_{1/2}\pi^+_{1/2})S' \leftrightarrow (\pi^-_{3/2})^2(\sigma^+_{1/2})^2S''$ in the perturbation theory. This coupling becomes prominent in the large S region. Owing to this additional contribution of the spin-triplet pairing, the mixture of the $2\hbar\omega$ states strongly occurs at a large distance region outside the crossing point, $S \geqslant 3.6$ fm. As a result of this coupling effect, in the 0^+_1 state, a total amount of the amplitude of the $2\hbar\omega$ configuration exceeds that of the $0\hbar\omega$ one, as can be confirmed in Fig. 4.

In contrast to 0^+_1, a large amplitude of the $\mu = 2$ AS exists in the 0^+_2 state. When we notice the outer component, the $\mu = 2$ AS has the $0\hbar\omega$ configuration of $(\pi^-_{3/2})^2(\pi^-_{1/2})^2$, as can be seen in Fig. 2. Thus, the 0^+_2 state can be considered to have the character of the $0\hbar\omega$ state. However, a considerable mixing of $2\hbar\omega$ appears beyond $S = 4.2$ fm, and the component of $2\hbar\omega$ exceeds that of $0\hbar\omega$ at $S = 4.6$ fm. This means that, in the 0^+_2 state, the $0\hbar\omega$ and $2\hbar\omega$ configurations coexist especially in the outer region of $S \geqslant 4.2$ fm.

A common feature, which can be seen in both the 0^+_1 and 0^+_2 states, is that the squared amplitude of the $2\hbar\omega$ state is longer range than that of the $0\hbar\omega$ state. This long-range feature is originated from the extended shape of the $\sigma^+_{1/2}$ orbit along the α-α axis. As shown in Fig. 2, the optimal S for $(\pi^-_{3/2})^2(\sigma^+_{1/2})^2$ is shifted to the outer region in comparison with that of $(\pi^-_{3/2})^2(\pi^-_{1/2})^2$, and the former configuration gains the total energy in the outside region beyond the crossing point. Because the energy of $(\pi^-_{3/2})^2(\sigma^+_{1/2})^2$ gradually increases as the distance gets larger, the mixing of $2\hbar\omega$ occurs with a long-range tail in superposing S. Furthermore, at the external region of $S \geqslant 5.2$ fm, the strong coupling with asymptotic channel of $\alpha + {}^8\mathrm{He}_{\mathrm{g.s.}}$ occurs because, in GTCM calculation, the MO configuration smoothly connects to the asymptotic channels. This means that the $\alpha + {}^8\mathrm{He}_{\mathrm{g.s.}}$ correlation cannot be negligible in the energy levels of 0^+_1 and 0^+_2. A detailed investigation on the smooth connection of MO and the $\alpha + {}^8\mathrm{He}_{\mathrm{g.s.}}$ channel is shown in Ref. [31].

B. Analysis based on the ^{x}He + ^{y}He cluster pictures

In this section, we try to understand the 0^+_1 and 0^+_2 states based on a simple model similar to a binary cluster model, in which basis functions are restricted to He clusters with a ground configuration, such as $\alpha + {}^8\mathrm{He}_{\mathrm{g.s.}}$, ${}^6\mathrm{He}_{\mathrm{g.s.}} + {}^6\mathrm{He}_{\mathrm{g.s.}}$, and ${}^5\mathrm{He}_{\mathrm{g.s.}} + {}^7\mathrm{He}_{\mathrm{g.s.}}$. In addition to the ground He clusters, we include the neutrons' excitations in the composite He clusters: $\nu(0p_{3/2})^4 \leftrightarrow \nu(0p_{3/2})^2(0p_{1/2})^2$ for ^{8}He, $\nu(0p_{3/2})^2 \leftrightarrow \nu(0p_{1/2})^2$ for ^{6}He, and $\nu(0p_{3/2})^3 \leftrightarrow \nu(0p_{3/2})^2(0p_{1/2}) \leftrightarrow \nu(0p_{3/2})(0p_{1/2})^2$ for ^{7}He. The former two excitations are the pairing excitations, which are considered the main higher-order correlations in even nuclei.

In Sec. III B1, we show the results of the coupled channel calculations of the even-even clusters, $(\alpha + {}^8\mathrm{He}) + ({}^6\mathrm{He} + {}^6\mathrm{He})$, and the comparison with the work in Ref. [13] is discussed. The energy surfaces of ${}^5\mathrm{He} + {}^7\mathrm{He}$ are investigated in Sec. III B2, and the importance of the odd-odd clusters is pointed out. The results of the 3 partitions with the pairing excitations are compared with the complete GTCM calculation in Sec. III B3.

1. *Solutions of* $(\alpha + {}^8\mathrm{He}) + ({}^6\mathrm{He} + {}^6\mathrm{He})$

The energy surfaces calculated with the $\alpha + {}^8\mathrm{He}$ and ${}^6\mathrm{He} + {}^6\mathrm{He}$ configurations including the pairing excitations are shown in Fig. 5. The energy of ${}^6\mathrm{He} + {}^6\mathrm{He}$ (dotted curve) has a similar shape to that of $\alpha + {}^8\mathrm{He}$ (dashed curve), although there is an energy shift by the thresholds. We can see the local minima around $S = 3.5$ fm in both cluster configurations. The clustering is more enhanced than that obtained in Ref. [13], where the energy minima are obtained at the shell-model limit of $S = 0$.

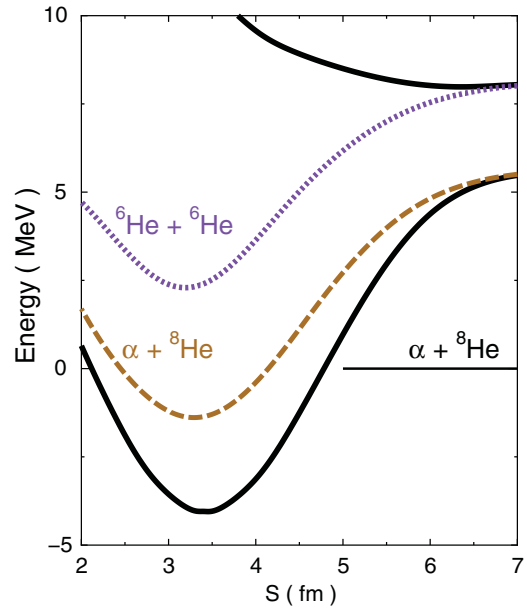

FIG. 5. (Color online) Energy surfaces of the even-even cluster configurations ($J^\pi = 0^+$). The dashed and dotted curves show the energy curves for $\alpha + {}^8\mathrm{He}$ and ${}^6\mathrm{He} + {}^6\mathrm{He}$, respectively. The solid curves represent the solutions of the coupled channels between them.

In our calculation, the parameter of the NN interaction is optimized for the model space including the $\alpha + {}^8\mathrm{He}$, ${}^6\mathrm{He} + {}^6\mathrm{He}$, and ${}^5\mathrm{He} + {}^7\mathrm{He}$ configurations and their intrinsic excitations (totally 38 channels). In contrast to the present model, the NN interaction is optimized only within two channels, such as $\alpha + {}^8\mathrm{He}_{\mathrm{g.s.}}$ and ${}^6\mathrm{He}_{\mathrm{g.s.}} + {}^6\mathrm{He}_{\mathrm{g.s.}}$, in the previous calculation [13]. In the setting of the present calculation, our interaction is obtained to be weaker for individual channels, and the cluster distance is much enhanced.

Strong energy shift occurs when the coupling between these cluster configurations is switched on. In the solid curves of Fig. 5, which is the solution of the coupled-channel calculation, the lowest minimum becomes much deeper than that of $\alpha + {}^8\mathrm{He}$, while the second minimum of ${}^6\mathrm{He} + {}^6\mathrm{He}$ disappears owing to the coupling effect. This means that the excited 0^+ state cannot exist close to the ground state in the model space of $(\alpha + {}^8\mathrm{He}) + ({}^6\mathrm{He} + {}^6\mathrm{He})$ with the pairing excitations.

2. *Solutions for* $(\alpha + {}^8\mathrm{He}) + ({}^6\mathrm{He} + {}^6\mathrm{He}) + ({}^5\mathrm{He} + {}^7\mathrm{He})$

We consider the effect of the odd-odd cluster, ${}^5\mathrm{He} + {}^7\mathrm{He}$, because the calculation of the even-even clusters is insufficient to reproduce a pair of minima in the energy surface. In Fig. 6, we show the energy surfaces of ${}^5\mathrm{He} + {}^7\mathrm{He}$ as a function of an α-α distance parameter. Because the intrinsic spins of ${}^5\mathrm{He}$ $(3/2^-)$ and ${}^7\mathrm{He}$ $(3/2^-)$ can couple to the channel spin $I = 0$ and 2 in an asymptotic region, there are two surfaces for ${}^5\mathrm{He} + {}^7\mathrm{He}$ (the dot-dashed curve for $I = 0$ and the solid one for $I = 2$). In the calculation of the energy, we include the excitation of valence neutrons in the $0p$ shell of ${}^7\mathrm{He}$, such as $\nu(0p_{3/2})^3 \to (0p_{3/2})^2(0p_{1/2}) \to (0p_{3/2})(0p_{1/2})^2$. The total of these neutrons' configurations couple to an intrinsic spin of 3/2. For a comparison with ${}^5\mathrm{He} + {}^7\mathrm{He}$, the energies for $\alpha + {}^8\mathrm{He}$ (dashed curve) and ${}^6\mathrm{He} + {}^6\mathrm{He}$ (dotted curves), which are the same as those shown in Fig. 5, are plotted in Fig. 6.

In the asymptotic region (large S), the two ${}^5\mathrm{He} + {}^7\mathrm{He}$ configurations with $I = 0$, 2 degenerate, and their energies are higher than those of the even-even cluster configurations. This is because a pair of neutrons are broken in ${}^5\mathrm{He} + {}^7\mathrm{He}$, and ${}^5\mathrm{He} + {}^7\mathrm{He}$ loses the neutrons' pairing energy. In the small α-α distance, the valence neutrons in ${}^{5,7}\mathrm{He}$ overlap and they interact with each other. Thus, the pairing energy among four neutrons is recovered, and the energy minima of ${}^5\mathrm{He} + {}^7\mathrm{He}$ are comparable to those of $\alpha + {}^8\mathrm{He}$ and ${}^6\mathrm{He} + {}^6\mathrm{He}$. Therefore, the coupling with the odd-odd cluster configuration becomes important in the interaction region.

To see the coupling effect between the even-even partitions and the odd-odd ones more clearly, in Fig. 7 we compare the energy curves calculated with the different model spaces: two partitions of $(\alpha + {}^8\mathrm{He}) + ({}^6\mathrm{He} + {}^6\mathrm{He})$ (dotted curves) and 3 partitions of $(\alpha + {}^8\mathrm{He}) + ({}^6\mathrm{He} + {}^6\mathrm{He}) + ({}^5\mathrm{He} + {}^7\mathrm{He})$ (solid ones). In this calculation, the internal excitations of ${}^{6-8}\mathrm{He}$ are mainly restricted to the neutrons' pairing excitations $[\nu(0p_{3/2})^2 \to (0p_{1/2})^2]$ as we have seen in the previous sections.

In the lowest surface, the energy minimum becomes lower as the model spaces are increased in the calculation. Moreover, we can see the distinctive difference in the comparison of the dotted curves with the solid ones. In the solid curve calculated by the restricted 3 partitions, local minimum is generated in the excited curve, while there is no minimum in the excited curve of the 2 partitions (dotted curve). This result means that the coupling with ${}^5\mathrm{He} + {}^7\mathrm{He}$ is important in the formation of a pair

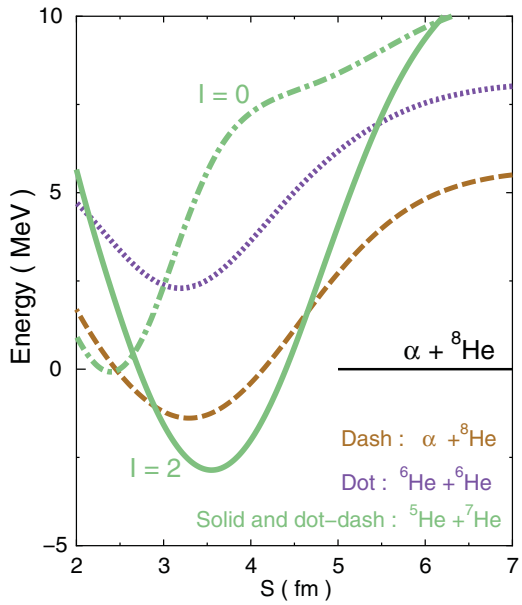

FIG. 6. (Color online) Comparisons of the energy surfaces for the cluster configurations of ${}^x\mathrm{He} + {}^y\mathrm{He}$ $(J^\pi = 0^+)$. The dashed and dotted curves represent the energy of $\alpha + {}^8\mathrm{He}$ and ${}^6\mathrm{He} + {}^6\mathrm{He}$, respectively, while the solid and dot-dashed ones represent the result of ${}^5\mathrm{He} + {}^7\mathrm{He}$ with $I = 2$ and $I = 0$, respectively.

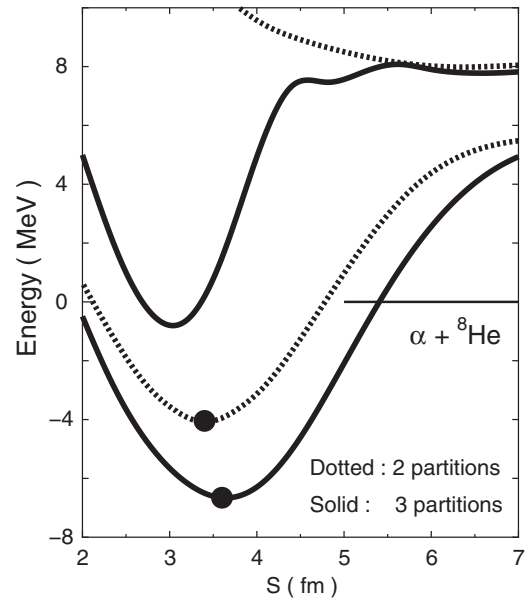

FIG. 7. Comparisons of the energy surfaces calculated by the various cluster configurations $(J^\pi = 0^+)$. The dotted and solid curves represent the results of the coupled channel calculation of $(\alpha + {}^8\mathrm{He}) + ({}^6\mathrm{He} + {}^6\mathrm{He})$ and $(\alpha + {}^8\mathrm{He}) + ({}^6\mathrm{He} + {}^6\mathrm{He}) + ({}^5\mathrm{He} + {}^7\mathrm{He})$, respectively. The solid circles show the minimum points. The dotted curves are the same as those shown in Fig. 5.

of two minima for the low-lying 0^+ states qualitatively. This is consistent with the results in the previous sections, showing the superiority of the MO picture, in which $(\alpha + {}^8\mathrm{He}) + ({}^6\mathrm{He} + {}^6\mathrm{He}) + ({}^5\mathrm{He} + {}^7\mathrm{He})$ are coherently mixed with each other, to describe the low-lying 0^+ states.

3. Comparison of the cluster picture with GTCM

The coupled channels of the 3 partitions plus the neutrons' excitation reproduce the results of the complete GTCM qualitatively. The comparison of the 3 partitions with the complete GTCM calculation is shown in Fig. 8. Here the complete GTCM calculation (dotted curves) includes 38 AO bases, while the calculation of the 3 partitions (solid curves) corresponds to the coupled channel with 11 channels: two channels in $\alpha + {}^8\mathrm{He}$ with ${}^8\mathrm{He}[(0p_{3/2})^4 \rightarrow (0p_{3/2})^2(0p_{1/2})^2]$, three channels in ${}^6\mathrm{He} + {}^6\mathrm{He}$ with ${}^6\mathrm{He}[(0p_{3/2})^2 \rightarrow (0p_{1/2})^2]$, and six channels in ${}^5\mathrm{He} + {}^7\mathrm{He}$ with ${}^7\mathrm{He}[(0p_{3/2})^3 \rightarrow (0p_{3/2})^2(0p_{1/2}) \rightarrow (0p_{3/2})(0p_{1/2})^2]$.

The calculation with 11 channels can generate the double minima appearing in the complete GTCM calculation. To investigate the effect of ${}^5\mathrm{He} + {}^7\mathrm{He}$ more clearly, we decompose the total energy of the lowest energy surface into kinetic $\langle T \rangle$ and potential $\langle V \rangle$ energies, which are shown in Table IV. Here the total energy E_{tot} is defined by $E_{\mathrm{tot}} = \langle T \rangle + \langle V \rangle - E_{\mathrm{in}}$, where E_{in} denotes the summation of the internal binding energy of α and ${}^8\mathrm{He}_{\mathrm{g.s.}}$. Individual contributions are calculated for three kinds of partitions: 1 partition with $\alpha + {}^8\mathrm{He}$, 2 partitions with $(\alpha + {}^8\mathrm{He}) + ({}^6\mathrm{He} + {}^6\mathrm{He})$, and 3 partitions with $(\alpha + {}^8\mathrm{He}) + ({}^6\mathrm{He} + {}^6\mathrm{He}) + ({}^5\mathrm{He} + {}^7\mathrm{He})$.

The absolute value of $\langle V \rangle$ decreases by about 2–3 MeV as the partitions increase ($1 \rightarrow 2 \rightarrow 3$), because the neutrons'

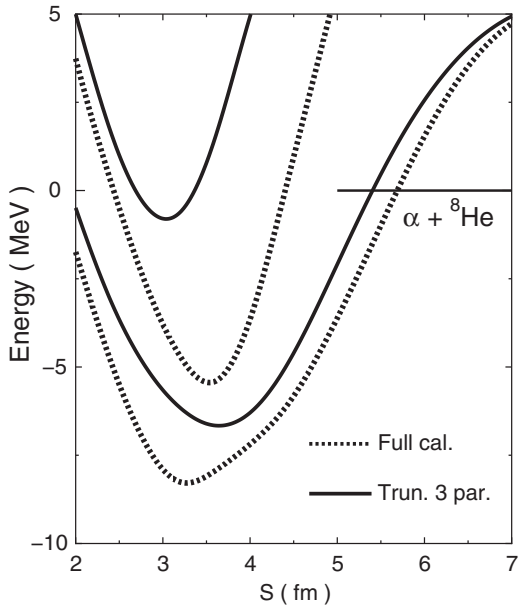

FIG. 8. Comparisons of the energy surfaces of the restricted cluster configurations with those of the full AESs ($J^\pi = 0^+$). The solid curves represent the results obtained by the coupled channels of the restricted clusters, while the dotted ones represent those of the full GTCM calculation.

TABLE IV. The expectation values of kinetic $\langle T \rangle$ and potential energies $\langle V \rangle$ with respect to the clusters' internal energy E_{in} at the minimum points S_{min} in the lowest energy surface. The result of "1 partition" represents the calculation with the single partition of $\alpha + {}^8\mathrm{He}$, while "2 partitions" and "3 partitions" represent the result of $(\alpha + {}^8\mathrm{He}) + ({}^6\mathrm{He} + {}^6\mathrm{He})$ and $(\alpha + {}^8\mathrm{He}) + ({}^6\mathrm{He} + {}^6\mathrm{He}) + ({}^5\mathrm{He} + {}^7\mathrm{He})$, respectively. The latter two results correspond to the solid circles shown in Fig. 7. The "Correlated MO" represents the result obtained by the correlated MO basis, which is shown in Fig. 3, while "GTCM" represents the complete calculation. E_{tot} denotes the total binding energy of $\langle T \rangle + \langle V \rangle - E_{\mathrm{in}}$. All the values are shown in units of MeV. The optimal S values are also shown.

Surfaces	S_{min}	$\langle T \rangle$	$\langle V \rangle - E_{\mathrm{in}}$	E_{tot}
1 Partition	3.2	212.13	−213.69	−1.56
2 Partitions	3.4	207.33	−211.38	−4.05
3 Partitions	3.6	202.01	−208.67	−6.66
GTCM	3.2	193.98	−202.24	−8.26
Correlated MO	3.2	194.91	−202.73	−7.82

$(0p)^4$ configuration inside ${}^8\mathrm{He}$ is broken by the neutron's exchange to the other α particle. However, the kinetic energy is largely reduced by this neutron's rearrangement effect, and the optimal distances (S_{min}) between two α particles are also enhanced, which is also confirmed in Fig. 7 (solid circles). This is because the moving space for the valence neutrons is extended by including the neutrons' rearrangement channels. The reduction is about 5 MeV at intervals of 1 partition increase. In the result of the 3 partitions, the reduction of $\langle T \rangle$ overcomes the loss of potential energy. This result is consistent to that obtained in ${}^{10}\mathrm{Be}$ [14], but the magnitude of the energy gain is much larger in ${}^{12}\mathrm{Be}$ than that in ${}^{10}\mathrm{Be}$.

The system gains total binding energy by the neutrons' rearrangements, but the energy surfaces obtained by the 3 partitions (11 channels) considerably deviate from the AESs of the complete GTCM in the whole region, as can be confirmed in Fig. 8. The deviations at the optimal distances amount to about 2 and 5 MeV for the lowest and second surfaces, respectively. In the energy decomposition for the lowest surface of GTCM, shown in Table IV (the second row from the bottom), the further reduction of $\langle T \rangle$ and loss of $\langle V \rangle$ appears at the minimum point by comparison with the restricted 3 partitions. The reduction of $\langle T \rangle$ reaches about 8 MeV, while the loss of $\langle V \rangle$ is about 6.4 MeV. This result means that, in the calculation of the restricted 3 partitions, sufficient reduction of the kinetic energy cannot be obtained although such a reduction is partially included in the neutrons' rearrangements.

In the restricted calculation, the neutrons' configurations are limited mainly to the pairing excitation, which keeps the neutrons' distributions spherical around one of the α cores. Such spherical distributions around one side cannot necessarily give a sufficient reduction of the neutrons' kinetic energy in the two-center system of $\alpha + \alpha$, which has a strongly deformed prolate shape. This is because, in a total of the neutrons' distribution, a nonsmoothing neck is always formed by the contact of two spherical nuclei.

On the contrary, in Fig. 3, we have found that the calculation with the correlated MO basis can nicely reproduce the energies of the full GTCM calculation for the whole distance. The largest energy difference is only about 0.4 MeV at the optimal distance of $S = 3.2$ fm. The decomposition of the total energy obtained by the correlated MO calculation is shown in the lowest row of Table IV. Both $\langle T \rangle$ and $\langle V \rangle$ nicely reproduce the individual contributions of GTCM. In the MO picture, therefore, the kinetic energy is sufficiently reduced. In the ground state, a dominant MO is $\sigma^+_{1/2}$. Because this orbit is strongly elongated along two α cores, it has a smooth distribution conforming to the $\alpha + \alpha$ shape. Such a smooth distribution leads to an extra reduction of kinetic energies for a neutron's orbit by comparison with a neck distribution with two spherical nuclei, corresponding to the 3 partitions plus the pairing excitations.

C. Rotational band structures

In this section, we extend the calculation of GTCM, which is similar to the calculation in Sec. III A3, to the finite spin J, and the rotational band structure is mainly investigated. Here the intrinsic K quantum number in Eq. (4) is restricted to zero, and the range of S is taken to be 1.2–8.8 fm with a mesh of $\Delta S = 0.4$ fm. The maximum spin of the bands gives an important information on the breaking of $N = 8$ magic number. In the naive shell model, the spins at the band termination are $J^\pi = 2^+$ and $J^\pi = 8^+$ for $\nu(0p)^6$ and $\nu(0p)^4(1s0d)^2$, respectively.

First, the band structures are calculated by the restricted basis of He clusters. In Fig. 9, the solid lines show the rotational bands obtained by solving the restricted coupled-channels of the 3 partitions plus the neutrons' excitations in $^{6-8}$He. In the $J^\pi = 8^+$ state, the local minimum of the energy surface becomes quite shallow, and the resultant energy level strongly couples to the continuum state. Owing to the coupling with the continuum, it is difficult to identify the level as a physical state. Thus, we do not show this state in the figure. In this figure, the experimental data are also shown by the diamonds [9], the double triangle [10], the solid triangle [7], and the cross [32]. The experimental data in parentheses represent the tentative spin assignment, and the data shown by the cross is plotted with respect to the $^6\mathrm{He}_{\mathrm{g.s.}} + {}^6\mathrm{He}_{\mathrm{g.s}}$ threshold.

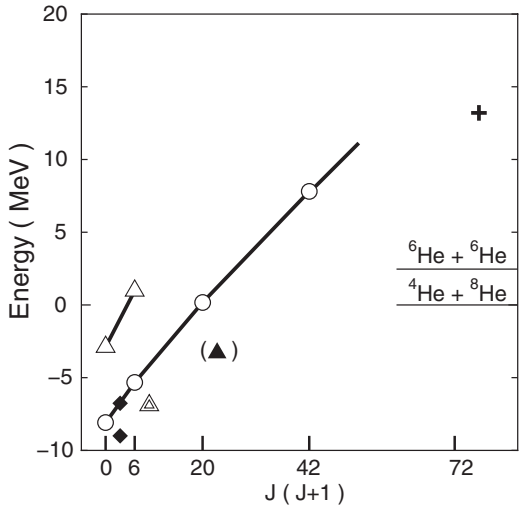

FIG. 9. Comparison of the restricted coupled-channels among the $\alpha + {}^8$He, ^{6}He + ^{6}He, and ^{5}He + ^{7}He clusters with the experimental spectra. The diamonds and the double triangles are taken from Refs. [9,10], respectively, while the solid triangles and the cross are from the data in Refs. [7,32]. The parentheses represent the tentative spin assignment.

TABLE V. Energies of the yrast bands and the 0^+_2 state. The energy of 0^+_1 is measured from the $\alpha + {}^8\mathrm{He}_{\mathrm{g.s.}}$ threshold, while the other values represent the excitation energies from the 0^+_1 state. "He cluster" and GTCM mean the calculation of the restricted 3 partitions and the complete GTCM, respectively. The deviation of the threshold energy of $^6\mathrm{He}_{\mathrm{g.s.}} + {}^6\mathrm{He}_{\mathrm{g.s.}}$ from the experiment (∼1.3 MeV shown in Table I) is added to the energy with the asterisk (20.9 + 1.3). All the energies are written in units of MeV.

	0^+_1	0^+_2	2^+	4^+	6^+	8^+
He-cluster	−8.1	5.2	2.8	8.3	15.9	–
GTCM	−9.3	2.1	3.0	7.7	13.9	21.8
Experiment	−9.0	2.2	2.1	5.7	–	22.2*

In the second row of Table V, the calculated energy values of the yrast bands and 0^+_2 are shown. Here the level of $J^\pi = 8^+$ is not shown owing to the coupling with the continuum. The 0^+_1 state is a little underbinding (about 1 MeV) by comparison with the experiment (lowest row) but the difference is prominent in the 0^+_2 and the high spin region of the ground band; the energy deviation for 0^+_2 amounts to about 3 MeV, while that for the $J^\pi = 4^+$ state is about 2.6 MeV. Therefore, the energy gain for the low-lying states is not sufficient in the calculation of the restricted 3 partitions, as we have pointed out in Sec. III B3, where the reduction effect of the kinetic energy is investigated.

Second, we show the rotational bands obtained by the complete GTCM calculation in Fig. 10. Because the GTCM calculation can be perfectly simulated by the correlated MO basis, as we have proven in Fig. 3 and Table IV, the bands calculated by the correlated MO bases are almost identical to the bands calculated by the complete GTCM in Fig. 10. The intruder MO, $(\pi^-_{3/2})^2(\sigma^+_{1/2})^2$ with the maximum spin of $J^\pi = 8^+$, becomes dominant in the ground band (circles) when the spin-triplet correlation discussed in Sec. III A1 is taken into account. Furthermore, the difference of the energies between the calculated bands and the observed spectra is improved, and the observed energy-spin systematics is nicely reproduced. In particular, the $J^\pi = 8^+$ state, which is not clearly identified in the binary He cluster treatment, is obtained just at the observed energy position by the full GTCM calculation. In

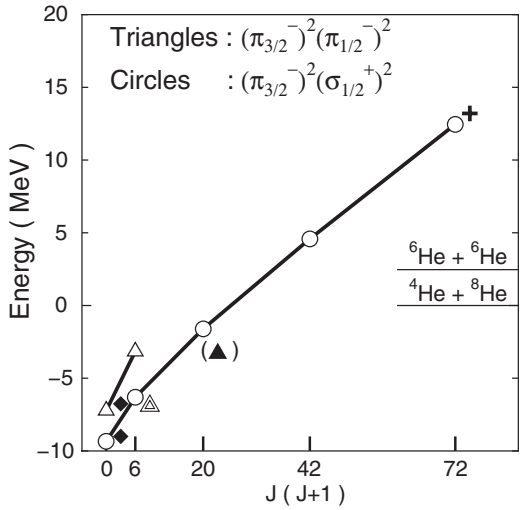

FIG. 10. Bands of the full GTCM calculation. The white symbols show the dominant component in individual bands. The diamonds, triangles, and cross represent the experimental data taken from Refs. [7,9,10,32].

the calculation with the correlated MO basis, a definite local minimum appears in $J^\pi = 8^+$ in contrast to the calculation with the restricted He-cluster basis. Therefore, the $J^\pi = 8^+$ state can be clearly identified as a physical state.

The binding energy of 0_1^+ and the excitation energies of the yrast band are shown in the third row of Table V. The deviation between the calculated energies and the experimental ones is smaller than about 2 MeV. These results mean that the correlated "MO" structures can explain the dominance of the intruder MO state of $(\pi_{3/2}^-)^2(\sigma_{1/2}^+)^2$ configuration in the ground state, which leads to the breaking $N = 8$ magic number. Unfortunately, experimental information in the high spin region ($J^\pi \geqslant 4^+$) is still lacking. Thus, to discuss the breaking of the magic number more deeply, identifying the energy levels and their spins in the region of $J^\pi \geqslant 4^+$ is strongly desired.

IV. SUMMARY AND DISCUSSION

In summary, we have studied the lowest two MO configurations, which are important for the low-lying 0^+ states, and explored mechanism for quenching $N = 8$ closure in the ^{12}Be nucleus from the viewpoint of two different pictures based on the cluster model: the covalent MO picture and the ionic He-cluster one. For this purpose, we have introduced a microscopic model, the GTCM [17,18]. In this model, it is possible to describe both the covalent and the ionic features of systems with two inert cores plus valence nucleons, because all partitions of valence nucleons are explicitly taken into account.

We explored the structure of the energy surfaces for the $J^\pi = 0^+$ states and showed channel coupling schemes. In the covalent MO picture, a competition between $(\pi_{3/2}^-)^2(\pi_{1/2}^-)^2$ and $(\pi_{3/2}^-)^2(\sigma_{1/2}^+)^2$, which correspond to the normal $\nu(0p)^6$ and $\nu(0p^4)(1s0d)^2$ configurations, respectively, occurs in the energy surface. The correlation of the spin-triplet pairing mainly gives rise to the binding-energy gain for the latter configuration, while the correlations for the former configuration can be negligible. As a result of the spin-triplet correlation, the energy difference between these two configurations is reduced, and a pair of two 0^+ states are naturally obtained.

On the contrary, a pair of the 0^+ states is not obtained in the coupled channel between $\alpha + {}^8$He and ^{6}He + ^{6}He. This result means that the full solutions with the pair 0^+ state cannot be simulated by a simple coupled channel of the cluster basis with the even-even partitions. The energies of ^{5}He + ^{7}He are higher than those of the even-even clusters in the asymptotic region owing to breaking the neutrons' pair but, in the interaction region, the pairing interaction between one neutron in ^{5}He and three neutrons in ^{7}He recovers. As a result of this recovery of the pairing interaction, the energies of ^{5}He + ^{7}He become almost the same as in the even-even clusters, and coherent coupling among ^{5}He + ^{7}He and the even-even states occurs. This coherent coupling plays an important role in the formation of the pair of 0^+ levels in the low-lying region.

In the formation of the low-lying states in ^{12}Be, the MO model gives a nice picture as expected in the studies of the MO model for ^{10,12}Be [14,15]. The superiority of the MO basis is consistent with the coherent mixing among the odd-odd clusters and the even-even ones because the MO configurations are always constructed by linear combinations of possible neutrons' partitions. This means that not only even-even clusters, which have already been considered in previous binary cluster models, but also odd-odd ones must be taken into account in handling MO structures of neutron excess systems. In both the MO and the He-cluster pictures, a common mechanism for a binding energy gain is reduction of the neutrons' kinetic energy. In the MO picture, $\sigma_{1/2}^+$ enhances the α-α clustering, and the kinetic energy is reduced by a formation of smooth neutrons' distribution conforming to a well-developed two-α distribution. In the binary He-cluster picture, different partitions strongly couple to each other because the MO configuration is optimal for the total system. This coupling increases the moving space of neurons and leads to the reduction of kinetic energy.

The competition between $(\pi_{3/2}^-)^2(\sigma_{1/2}^+)^2$ and $(\pi_{3/2}^-)^2(\pi_{1/2}^-)^2$ is also confirmed in the formation of the rotational band structures. Owing to the spin-triplet pairing correlation, the former state becomes the yrast band. In the He-cluster picture, the inclusion of the ^{5}He + ^{7}He states plays an important role for the inversion of the lowest two rotational bands.

It is instructive to compare the present calculation of the cluster basis with that in Ref. [13]. The ground band in Ref. [13] corresponds to the simple $\nu(0p)^6$ shell-model limit (zero α-α distance) of $\alpha + {}^8\text{He}_{\text{g.s.}}$ and $^6\text{He}_{\text{g.s.}} + {}^6\text{He}_{\text{g.s.}}$ and the ground band terminates at $J^\pi = 2^+$. However, the clustering is enhanced in the present model, and a maximum spin of the present ground band goes beyond $J^\pi = 2^+$. This result means that the $\nu(0p)^6$ configuration is broken in the present cluster model. In the present calculation, the NN interaction is optimized in larger model space than that in Ref. [13]. The difference on the ground band property could be attributed to a setting of the model space in the calculations and the

effective NN interaction optimized in the employed model space.

Our global subject is a unified study from bounds to continuum but, in the present study, we focused on the properties of the yrast and first excited bands. By employing GTCM, which can handle both MO structures and their separation to binary cluster structures, we have confirmed that the MO picture works nicely for the low-lying yrast bands. In our recent studies, however, we have pointed out a possibility that the other structures, such as the binary cluster structures, are favored in a continuum energy region [19–21,33]. Above the α decay threshold, prominent resonances, strongly decaying into $^6\mathrm{He}_{\mathrm{g.s.}} + {}^6\mathrm{He}_{\mathrm{g.s.}}$ and $\alpha + {}^8\mathrm{He}_{\mathrm{g.s.}}$, were observed [32,34,35]. Therefore, extending the present studies to the highly excited region, where the coupling to the scattering continuum plays important roles, is interesting. A detailed analysis on the continuum states of ^{12}Be is now under way.

ACKNOWLEDGMENTS

The authors would like to thank Professor K. Katō, Professor T. Nakatsukasa, and Professor T. Yamada for useful discussions and encouragement. This work has been supported by a Grant-in-Aid for Scientific Research in Japan (No. 18740129 and No. 19740124). The authors would also like to thank the JSPS core-to-core program. The numerical calculations have been performed at the RSCC system, RIKEN.

[1] K. Ikeda *et al.*, Suppl. Prog. Theor. Phys. **68**, 1 (1980), and references therein.
[2] M. Ito, Y. Sakuragi, and Y. Hirabayashi, Eur. Phys. J. (1999); Phys. Rev. C **63**, 064303 (2001); M. Ito, Y. Hirabayashi, and Y. Sakuragi, *ibid.* **66**, 034307 (2002).
[3] A. Thosaki, H. Horiuchi, P. Schuck, and G. Röpke, Phys. Rev. Lett. **87**, 192501 (2001); Y. Funaki, A. Thosaki, H. Horiuchi, P. Schuck, and G. Röpke, Phys. Rev. C **67**, 051306(R) (2003).
[4] T. Yamada, Y. Funaki, H. Horiuchi, K. Ikeda, Y. Funaki, and A. Thosaki, Prog. Theor. Phys. **120**, 1139 (2008).
[5] Y. Kanada-Enýo, H. Horiuchi, and A. Ono, Phys. Rev. C **52**, 628 (1995); Y. Kanada-Enýo and H. Horiuchi, *ibid.* **55**, 2860 (1997), and references therein.
[6] H. Iwasaki *et al.*, Phys. Lett. B **481**, 7 (2000).
[7] H. G. Bohlen *et al.*, J. Phys. Conf. Ser. **111**, 012021 (2008).
[8] H. Iwasaki *et al.*, Phys. Lett. B **491**, 8 (2000).
[9] S. Shimoura *et al.*, Phys. Lett. B **560**, 31 (2003).
[10] S. Shimoura *et al.*, Phys. Lett. B **654**, 87 (2007).
[11] M. Ito and Y. Sakuragi, Phys. Rev. C **62**, 064310 (2000).
[12] P. Descouvemont and D. Baye, Few-Body Syst. **29**, 131 (2000).
[13] P. Descouvemont and D. Baye, Phys. Lett. B **505**, 71 (2001).
[14] N. Itagaki, S. Okabe, and K. Ikeda, Phys. Rev. C **62**, 034301 (2000), and references therein.
[15] N. Itagaki and S. Okabe, Phys. Rev. C **61**, 044306 (2000).
[16] Y. Kanada-En'yo and H. Horiuchi, Phys. Rev. C **68**, 014319 (2003).
[17] M. Ito, K. Kato, and K. Ikeda, Phys. Lett. B **588**, 43 (2004).
[18] Makoto Ito, Phys. Lett. B **636**, 293 (2006); Mod. Phys. Lett. A **21**, 2429 (2006).
[19] M. Ito, N. Itagaki, H. Sakurai, and K. Ikeda, Phys. Rev. Lett. **100**, 182502 (2008); J. Phys. Conf. Ser. **111**, 012010 (2008).
[20] M. Ito and N. Itagaki, Phys. Rev. C **78**, 011602(R) (2008); Int. J. Mod. Phys. E **17**, 2061 (2008).
[21] M. Ito and N. Itagaki, Phys. Rev. Focus **22** Story 4 (2008); Riken Res. **3**, 9 (2008).
[22] Makoto Ito, Int. J. Mod. Phys. A **24**, 2175 (2009); M. Ito and N. Itagaki, Mod. Phys. Lett. A **24**, 1005 (2009).
[23] M. Ito and D. Suzuki, Phys. Rev. C **84**, 014608 (2011).
[24] M. Pervin, S. C. Pieper, and R. B. Wiringa, Phys. Rev. C **76**, 064319 (2007); K. M. Nollett, S. C. Pieper, R. B. Wiringa, J. Carlson, and G. M. Hale, Phys. Rev. Lett. **99**, 022502 (2007), and references therein.
[25] P. Navrátil, C. A. Bertulani, and E. Caurier, Phys. Rev. C **73**, 065801 (2006); P. Navrátil and W. E. Ormand, *ibid.* **68**, 034305 (2003); Phys. Rev. Lett. **88**, 152502 (2002).
[26] H. Horiuchi *et al.*, Suppl. Prog. Theor. Phys. **62**, 1 (1977).
[27] D. M. Brink, in *Proceedings of the International School of Physics Enrico Fermi Course XXXVI*, edited by C. Bloch (Academic, New York, 1966), p. 247.
[28] P. Ring and P. Schuck, *Nuclear Many-Body Problem*, 1st ed. (Springer-Verlag, Berlin Heidelberg, New York, 2004), p. 476.
[29] A. B. Volkov, Nucl. Phys. **74**, 33 (1965).
[30] N. Yamaguchi, T. Kasahara, S. Nagata, and Y. Akaishi, Prog. Theor. Phys. **62**, 1018 (1979).
[31] Makoto Ito, Phys. Rev. C **83**, 044319 (2011).
[32] M. Freer *et al.*, Phys. Rev. C **63**, 034301 (2001); Phys. Rev. Lett. **96**, 042501 (2006).
[33] M. Ito and K. Yabana, Prog. Theor. Phys. **113**, 1047 (2005).
[34] A. A. Korsheninnikov *et al.*, Phys. Lett. B **343**, 53 (1995).
[35] A. Saito *et al.*, AIP Conf. Proc. **891**, 205 (2006); Mod. Phys. Lett. A **25**, 1858.